

# 1 Late Pleistocene – Holocene denudation, uplift, and morphology evolution of the Armorican Massif (western 2 Europe)

3

4 Malcles, O. <sup>1</sup>, Mazzotti S. <sup>1</sup>, Vernant P. <sup>1</sup>, Godard V. <sup>2</sup>

5 1. Géosciences Montpellier, Université de Montpellier, CNRS

6 2. CEREGE, Aix Marseille Univ., CNRS, IRD, INRA, Coll. France

7 Correspondence to: Oswald Malcles (oswald.malcles@hotmail.fr)

8

## 9 Abstract

10 Elevated Plio-Pleistocene coastal and marine markers in stable continental regions are commonly explained by  
11 a combination of eustatic sea-level variations and large-scale geological processes (e.g., crustal or mantle dynamics). In  
12 this study, we test the role of erosion rates on the Late Pleistocene uplift and landform evolution of the Armorican  
13 Massif, western France. Denudation rates are estimated for 19 drainage basins using terrestrial cosmogenic nuclide  
14 (<sup>10</sup>Be) measurements in quartz. They range between 3 and 27 m.Ma<sup>-1</sup>, with a factor of two difference between the  
15 western highland region and the central lowland region (13 ± 6 m.Ma<sup>-1</sup> vs. 7 ± 4 m.Ma<sup>-1</sup>). Assuming a thin elastic plate  
16 model, the lithosphere flexural isostatic response to these denudation rates produces an overall uplift rate of the  
17 Armorican Peninsula from 12–15 m.Ma<sup>-1</sup> in the central lowland region to 4–10 m.Ma<sup>-1</sup> in the western peninsula and  
18 along the coastline. We show that these erosion-driven uplift rates can explain the uplifted Late Pleistocene marine  
19 terraces along the Armorican Peninsula coastline as well as the elevated Quaternary marine deposits in the central  
20 lowland region, without necessitating additional geodynamic processes such as regional compression or local active  
21 faults. Our results suggest that, in stable continental regions, long-term erosion should be taken into account as a  
22 driver of uplift and deformation before trying to derive global or regional geodynamic or tectonic conclusions.

23

## 24 1. Introduction

25 Plio-Pleistocene uplift rates ca. 10 – 100 m · Ma<sup>-1</sup> are observed in numerous stable continental regions, i.e., in  
26 areas unaffected by direct plate-boundary processes (e.g., Australia, South Africa, northwestern Europe). Most of  
27 these uplift rates are derived from elevated coastal or alluvial landforms, such as marine terraces, planation surfaces  
28 (rasas) or river terraces, and from sedimentary records, such as raised beaches or endo-karstic infilling. The origins of  
29 these slow coastal uplift rates are debated (e.g., Erlanger et al., 2012) and have been attributed to a large variety of  
30 geodynamic processes: global mantle dynamics (Gurnis et al., 2000) or plate tectonics (Pedoja et al., 2011), regional  
31 lower crustal flow triggered by glaciation cycles (Westaway et al., 2002), local fault reactivation (Bonnet et al., 2000),  
32 or local volcanism (Murray-Wallace et al., 1996). Surprisingly, none of these studies consider the role of long-term  
33 erosion as a potential driver of coastal uplift through simple isostatic adjustment.

34 Here, we address the relationship between long-term erosion rates, uplift rates, and landform evolution of  
35 the Armorican Massif, western France (Fig. 1) during the Late Pleistocene – Holocene epochs. This region comprises  
36 several coastal landforms and marine deposits that witness recent uplift of the whole area, including indications of  
37 spatial uplift variations that may reflect local fault reactivation (cf. Section 2). In addition to numerous uplift rate data,

the Armorican Massif offers several specific advantages for testing the role of erosion in local and regional uplift: Due to its peculiar geography, it is only affected by local erosion. Mass redistribution from regional inland sources is not possible due to the watershed geometry, and offshore processes (e.g., talus deposits) are negligible due to their low long-term magnitudes (cf. Section 4). The massif erosion pattern can be estimated by quantifying erosion rates at a spatial scale of a few tens of kilometers based on small watershed sampling, while keeping rather homogenous morphology (Fig. 2), lithology, production rates, etc. Finally, its geology consists primarily of quartz-rich basement and metasediment formations, which allow for estimations of denudation rates at the scale of drainage basins using terrestrial cosmogenic nuclide ( $^{10}\text{Be}$ ) measurements in quartz.

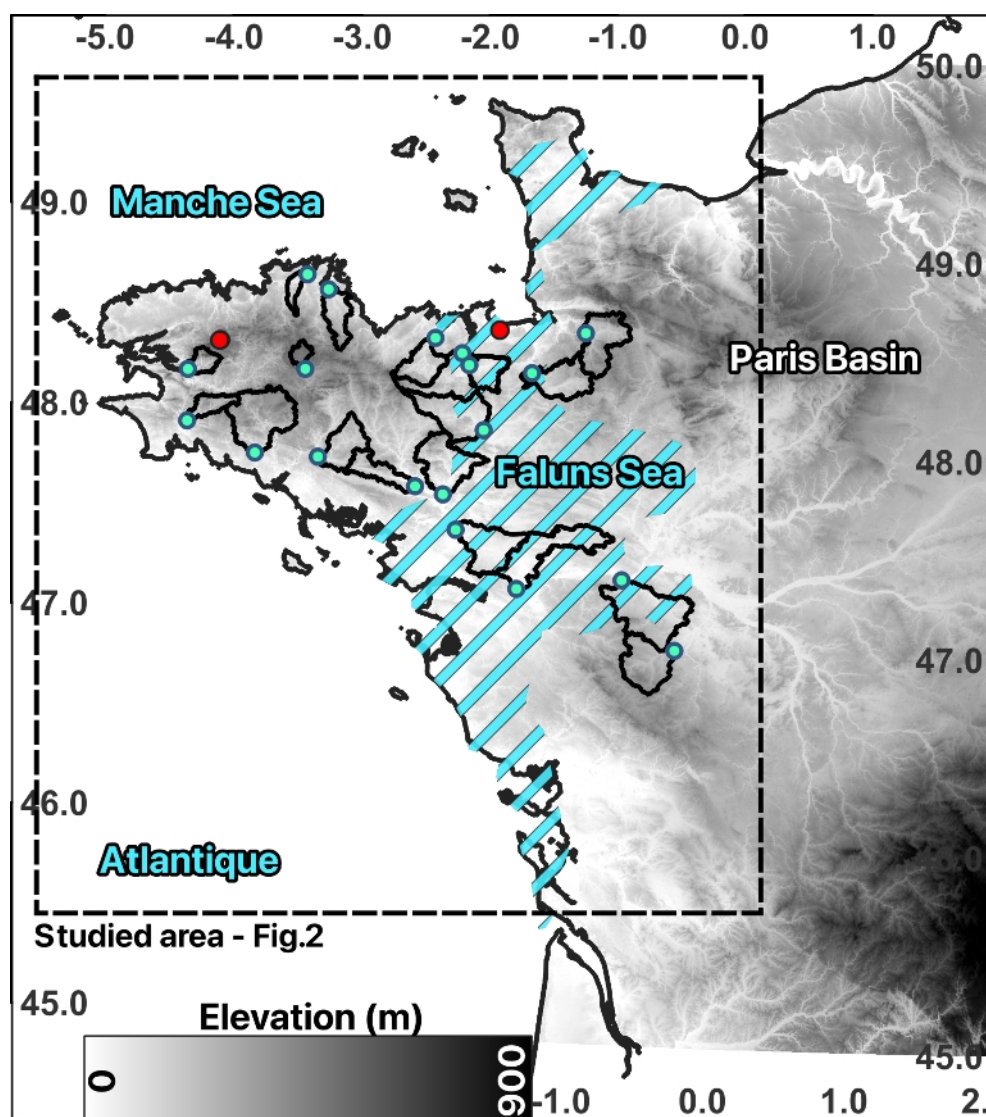


**Figure 1. Armorican Massif topographic map.** Green DEM from JAXA-ALOS W3D30. The studied watersheds are delimited by the black-contoured polygons with the sampling sites identified with the blue points. Outcrops sampling sites are marked by the red points. Blue stripes: approximate onshore extent of the Mio-Pliocene "Faluns Sea" (Néraudeau et al., 2010).

In the following, after a short description of the regional geological and geomorphological setting and evolution, we detail the sampling strategy and processing methodology to derive new denudation rates in 19 watersheds covering the Armorican Massif. These new data are then integrated within a regional Western European

database to construct denudation rate models for the whole Armorican Massif and neighboring areas, which then serve as inputs for models of uplift rates driven by flexural isostatic adjustment. Given the magnitudes and uncertainties in denudation rates, apparent uplift rates, and eustatic sea level corrections, our analyses show that Pleistocene–Holocene absolute uplift rates in the Armorican Massif can be explained by the flexural isostatic response to local denudation rates (at wavelengths of 50–100 km), without need for additional processes such as lithosphere bulging or local fault activity. Additional processes cannot be ruled out but, if present, must be significantly slower than previously proposed.



**Figure 2: Photography** of common landscape and sampling site types. A- Guindy river sampling site. Example of small scale anthropic disturbances. B- Meu river sampling site, view toward upstream. Example of surrounding flat topography with local river talus and generalized tree-covered landscape. C- Claie river sampling site. Another example of surrounding flat topography with local river talus and crops/bare ground. D- Example of localized relief, southern

Brittany. E- Roc'h-Ruiz: example of sampled outcropping rocks and shrub-land areas. F- Arguenon sample site. View toward downstream, example sampled central sand-bar. Photos: O. Malcles

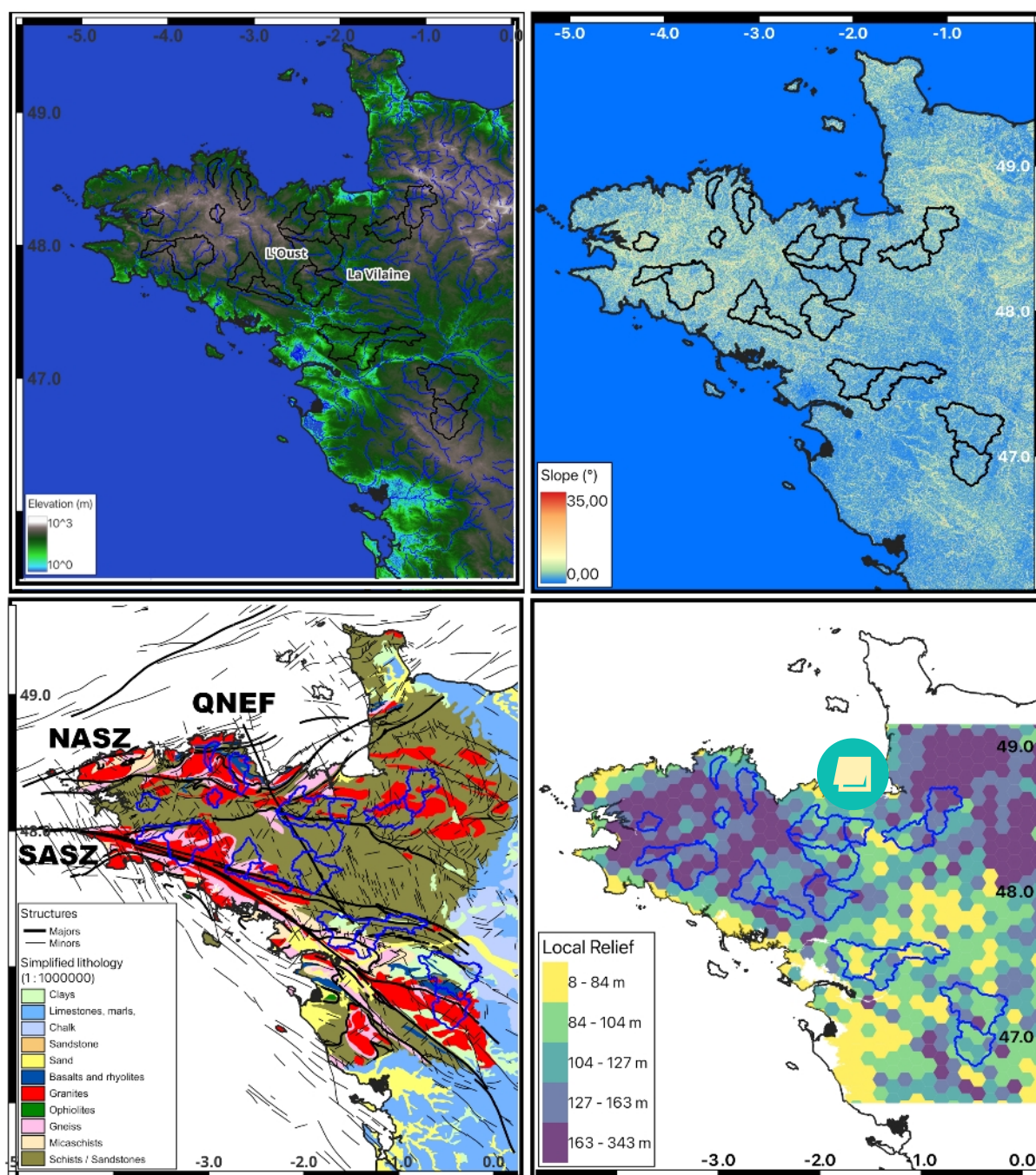
## 2. Geological and geomorphological setting

The Armorican Massif, western France, corresponds mostly to the remnant basement and structures of the Cadomian (650–540 Ma) and Variscan (370–300 Ma) orogens (Ballèvre et al., 2009). It comprises four main tectonic domains separated by major crustal-scale faults and shear zones (North-Armorican and South-Armorican Shear Zone systems), with other major fault systems also noticeable (e.g., Quessnoy-Nort-sur-Erdre Fault, QNEF, Fig. 3). Its Mesozoic geological history is marked by minor fault reactivations associated with far-field tectonic events (e.g., North Atlantic Ocean opening, Pyrenean orogeny, ...), up to the present-day moderate background seismicity indicating small ongoing deformation (Beucler et al., 2021). Overall, the Armorican Massif is primarily composed of Proterozoic and Paleozoic crystalline basement and metasediment formations, with limited remnants of Meso-Cenozoic sedimentary deposits. Studies of planation surfaces and stratigraphic constraints indicate at least two major phases of burial and exhumation during the mid-Mesozoic and the late-Cretaceous – early-Eocene (Bessin et al., 2014). The thicknesses of the associated sedimentary covers (and thus the eroded thicknesses) are poorly constrained but were probably limited to several hundred meters, based on the remaining deposits. Several later episodes of minor marine transgressions and sediment deposits occurred during the Cenozoic, up to the most recent Red Sands and Faluns associated with the “Faluns Sea” (Fig. 1) during the Upper Miocene – Pliocene (Guillocheau et al., 2003).

These Red Sands and Faluns formations correspond to two cycles of marine transgressions / regressions during the Upper Miocene (5–8 Ma) and the Upper Pliocene (2–3 Ma), with marine flooding limited to the present-day low-elevation regions of central Brittany and Normandy (Fig. 1). While the Faluns deposits are good markers for estimations of long-term uplift rates owing to their shallow-depth open-marine fauna, the Red Sands provide less robust uplift markers due to their complex nature of continental sheetflood, fluvial, and estuarine deposits (Néraudeau et al., 2003; Brault et al., 2004). Their sedimentary and stratigraphic characteristics point to a system of shallow-water marine transgressions between elevated continental domains, with an overall smooth topography and large braided rivers directly connected to numerous estuaries (Guillocheau et al., 2003; Brault et al., 2004). They also indicate a relatively high clastic discharge from two continental domains on both sides of main north-south divide (i.e., “West Armorican and North Cotentin islands” scenario). This Mio-Pliocene configuration changes during the Mid Pleistocene (ca. 1–1.5 Ma), with the disappearance of marine deposits and the formation of the present-day drainage network that incises into the Red Sands and Faluns formations. In contrast with the Mio-Pliocene system, the current (Pleistocene – Holocene) drainage network is characterized by incised valleys and jagged topography with a main east-west divide. The rivers tend to be spatially associated with tectonic scarps and structures (e.g., following the major NW-SE exhumed shear zones in southern Brittany), indicating either differential erosion along weaker inherited faults and shear zones, or a control by a potential recent reactivation of these structures (Bonnet et al., 1998, 2000).

These various Cenozoic marine deposits and landforms provide detailed information on the topographic evolution of different sectors of the Armorican Massif. Hereafter, we refer to “apparent uplift” when considering the elevation of paleo marine markers relative the present-day sea level due to a combination of eustatic sea level variation and vertical land movement, in contrast with “uplift” which is used to refer to vertical land motion (i.e., corrected for eustatic variations).

106 The marine Mio-Pliocene Faluns are found at present-day elevations between ca. 20 and 90 m. Assuming a  
 107 eustatic sea level highstand of 60 m during the Upper Pliocene (relative to present-day sea level) and based on ESR  
 108 (Electron Spin Resonance) dating, Brault et al. (2004) estimate an uplift of 12–40 m of the second maximum flooding  
 109 surface situated in the central low-elevation region of the Armorican Massif. This would correspond to an average  
 110 uplift rate in this area of  $4\text{--}13\text{ m}\cdot\text{Ma}^{-1}$  since ca. 3 Ma. This estimation is in rough agreement with those by Bessin et al.  
 111 (2017) based on a reanalysis of marine deposits and sea-level curves, which yield average Pleistocene uplift rates of  $16$   
 112  $\pm 2$  and  $29 \pm 2\text{ m}\cdot\text{Ma}^{-1}$  for the low-elevation regions of Brittany and Normandy. No uplift estimations exist for the high-  
 113 elevation domains.



114  
 115 **Figure 3: Top left:** Elevation map in a  $\log_{10}$  scale to highlight the regional pattern (DEM data from JAXA, river network  
 116 from ©OpenStreetMap, Distributed under the Open Data Commons Open Database License (ODbL) v1.0. The two main  
 117 basins (Oust and Vilaine) are located. Top right: slope map of the studied area. Bottom left: Simplified geological map

(wms data from BRGM: <http://geoservices.brgm.fr/geologie>). Main tectonic structures shown in black (SASZ: South Armorican Shear Zone; NASZ: North Armorican Shear Zone; QNEF: Quessoy-Nort-sur-Erdre Fault). Bottom right: relief calculated for the 100 km<sup>2</sup> hexagonal grid.

More recent estimations can be derived from the numerous Pleistocene marine terraces and rasas (sea-driven planation) that mark the coastline of Brittany and Normandy. Using the compilation of Pedoja et al. (2018), we estimate an average apparent uplift since MIS 5e (last interglacial, ca. 130 ka) of 6 m for western Brittany (31 terraces), 5 m for western Cotentin (7 terraces), and 8 m for the Channel Islands (4 terraces). These values are associated with an accuracy of 1–3 m based on the margin of error defined in Pedoja et al. (2018) and on the data standard deviations. The eustatic sea level highstand during MIS 5e was located between ca. 3 m (Siddall et al., 2007) and ca. 7.5 m (Dutton and Lambeck, 2012) above present-day sea level, leading to an uplift between -1.5 m and 3 m for western Brittany, -2.5 m and 2 m for western Cotentin, and 0.5 m and 5 m for the Channel Islands (negative uplift values indicate subsidence). Thus, the Late Pleistocene regional trend may correspond to a period of slow uplift rate (15–40 m · Ma<sup>-1</sup>) assuming a low eustatic highstand of 3 m, or a period of slow subsidence rate (-20–0 m · Ma<sup>-1</sup>) for a high eustatic highstand of 7.5 m. For the penultimate interglacial (MIS 11, ca. 400 ka), Pedoja et al. (2018) estimate an average apparent uplift of 20 m of western Europe marine terraces and rasas. Combined with a eustatic sea level highstand of 6–13 m (Muhs et al., 2012; Raymo and Mitrovica, 2012), this yields an average uplift rate of 18–35 m · Ma<sup>-1</sup> since 400 ka.

A few studies provide information on recent relative or absolute uplift rates in the Armorican Massif. Geomorphic analyses of river incisions and watershed morphologies indicate a differential uplift of ca. 30 m between western Brittany (Oust watershed) and central Brittany (Vilaine watershed) (Bonnet et al., 1998). A similar differential uplift of western Brittany relative to the central low-elevation area is deduced from numerical analyses of the topography and slope / drainage relationships (Lague et al., 2000). Assuming that this morphological difference is inherited from a differential uplift since the Pleistocene, these studies indicate a relative west / center uplift rate of ca. 10–15 m · Ma<sup>-1</sup>. Bonnet et al. (1998) propose a faster relative rate of 40–60 m · Ma<sup>-1</sup> based on archeological finds in one terrace on the northern coastline of the Oust watershed (lithic industry from the Cromerian stage, 0.7–0.5 Ma, Monnier et al., 1981). The leveling data analysis of Lenôtre et al. (1999) supports the relative west vs. center uplift, albeit at a differential rate of 1000 m · Ma<sup>-1</sup> (1 mm · a<sup>-1</sup>) or more. Recent results using GNSS (Global Navigation Satellite System) data show that this differential rate is likely overestimated, due to biases inherent to old leveling data, and that present-day vertical rates in the Armorican Massif are below the resolution of geodetic data, i.e., lower than ca. 500 m · Ma<sup>-1</sup> (0.5 mm · a<sup>-1</sup>) (Masson et al., 2019).

### 3. Denudation rates from terrestrial cosmogenic nuclide

#### 3.1. Drainage basin sampling and <sup>10</sup>Be measurements

To estimate denudation rates at the scale of drainage basins, we sampled quartz-rich river sands (plus a few gravel-to-cobble samples) and measured their concentrations of cosmogenic beryllium 10 (<sup>10</sup>Be), which is produced in quartz grains within the first few meters of the surface. This concentration is a function of the local surface production and denudation rates (e.g. Granger et al., 1996, Von Blanckenburg, 2005). Thus, <sup>10</sup>Be measurements in river sands provide an estimation of the mean upstream denudation rate above the sampling point, as long as the main

hypotheses of this method are respected (e.g., nearly homogeneous quartz content in the watershed). We collected samples in exposed sand pockets along riverbanks and on sand bars, avoiding as much as possible accumulation spots due to anthropic structures and alterations of the river channel. This constraint, and the fact that downstream river sections close to the coast are often filled with mud, limited our sampling to upstream sites. In total, we sampled 19 watersheds (Table 1, Fig. 1, 2, 3), three of which were sampled twice (a few meters apart) to estimate the repeatability between sand samples (Argenton, Layon, Leff). Three others were sampled with both sands and gravel-to-cobble sediment for comparison (Erdre, Douffine, Evel).

Sand and coarser samples followed a standard preparation procedure via crushing, sieving (retaining of the 250–1000  $\mu\text{m}$  fraction), leaching with  $\text{HCl} + \text{HNO}_3$  acids, magnetic separation, suppression of non-quartz grains using multiple  $\text{H}_2\text{SiF}_6$  baths, and final removal of the atmospheric  $^{10}\text{Be}$  by multiple  $\text{HF}$  etchings. From the purified quartz,  $\text{Be}$  was separated following Ruszkiczay-Rüdiger et al. (2021) via multiple ion exchange chromatography and selective pH precipitation following total dissolution and the addition of 250  $\mu\text{L}$  of known  $^9\text{Be}$  concentration solution. After separation,  $\text{Be}$  was oxidized at 800  $^\circ\text{C}$  and mixed with  $\text{Nb}$  (volumetric ratio  $\sim 1:1$ ) prior to measurement. The  $^{10}\text{Be}/^9\text{Be}$  concentration ratio was measured by accelerator mass spectrometry at the ASTER national facility (Arnold et al., 2010). The ratios were calibrated using ASTER standards (Braucher et al., 2015) to derive  $^{10}\text{Be}$  concentrations.

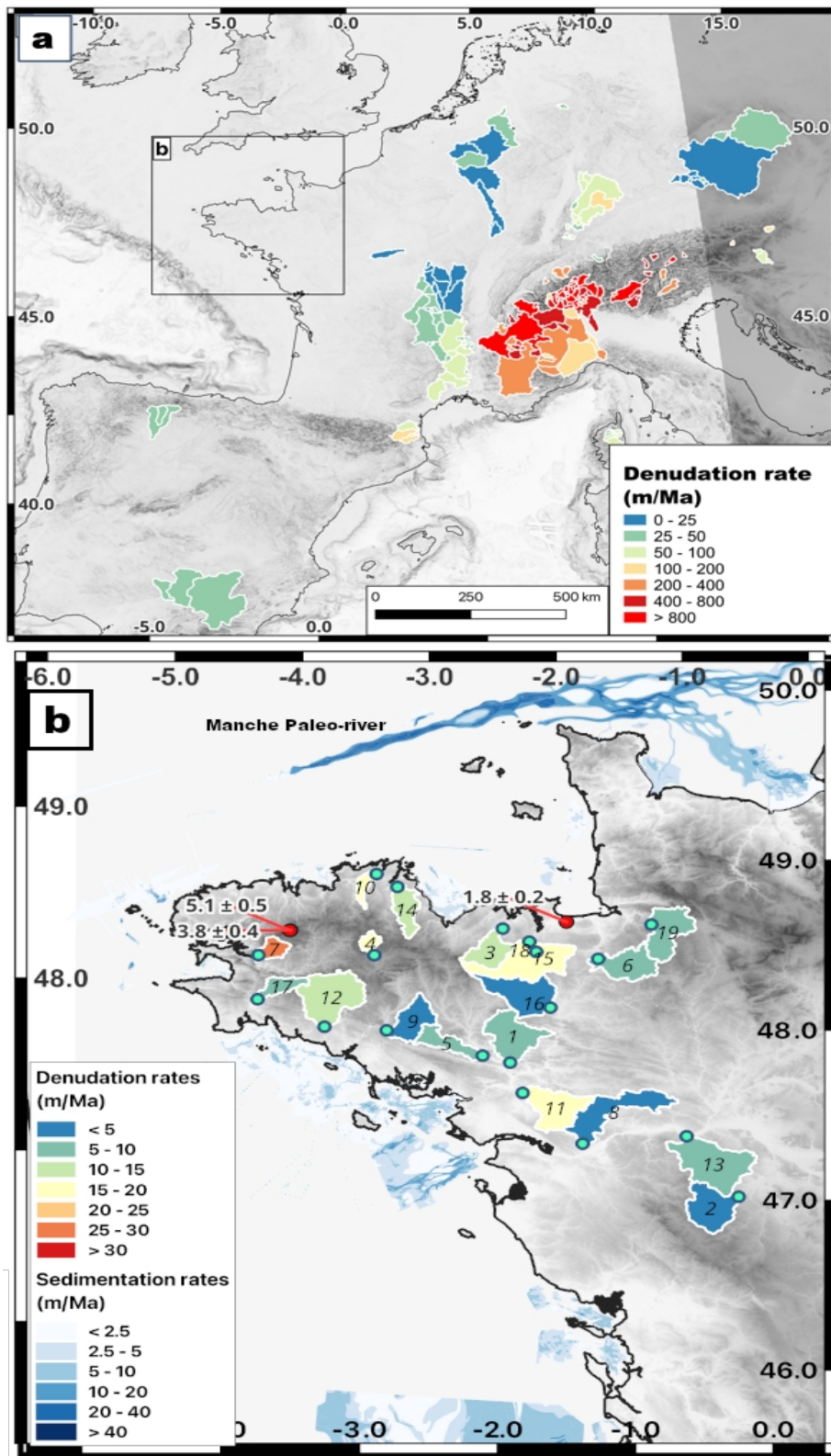
**Table 1. Armorican Massif TCN denudation rates and morphology parameters**

Name	area ( $\text{km}^2$ )	mean altitude (m)	mean slope ( $^\circ$ )	Relief (m)	HI	Mass Qz (g)	$^{10}\text{Be}/^9\text{Be}$ ( $10^{-13}$ )	$\text{C} \pm \sigma_c$ ( $10^5 \text{ atm.g}^{-1}$ )	$\text{d} \pm \sigma_d$ ( $\text{m} \cdot \text{Ma}^{-1}$ )
<b>Watersheds</b>									
(1) Aff	712	78	2.6	319	0.39	18.429	$1.14 \pm 0.04$	$3.77 \pm 0.15$	$7.6 \pm 0.7$
(2) Argen- ton	651	155	1.8	184	0.51	28.973	$3.59 \pm 0.13$	$7.77 \pm 0.31$	$3.6 \pm 0.3$
(2) Argen- ton				184		29.852	$2.00 \pm 0.09$	$0.42 \pm 0.22$	$7.2 \pm 0.7$
(3) Ar- guenon	416	98	2.5	328	0.28	18.535	$7.68 \pm 0.07$	$2.56 \pm 0.26$	$11.8 \pm 1.6$
(4) Blavet	112	254	2.8	155	0.67	31.654	$1.14 \pm 0.09$	$2.18 \pm 0.18$	$16.3 \pm 1.9$
(5) Claie	353	97	2.8	175	0.52	29.535	$1.43 \pm 0.06$	$3.03 \pm 0.15$	$9.8 \pm 0.9$
(6) Coues- non	558	113	2.3	229	0.41	29.669	$1.95 \pm 0.08$	$4.11 \pm 0.20$	$7.16 \pm 0.7$
(7) Douffine	173	155	5.0	362	0.41	30.371	$0.59 \pm 0.09$	$1.23 \pm 0.19$	$27 \pm 5$
(7) Douffine (c)				362		29.465	$1.47 \pm 0.09$	$3.12 \pm 0.21$	$10.1 \pm 1.1$
(8) Erdre	829	44	1.7	171	0.42	33.466	$3.30 \pm 0.10$	$9.32 \pm 0.33$	$2.6 \pm 0.3$
(8) Erdre (c)				171		20.561	$1.70 \pm 0.05$	$5.19 \pm 0.18$	$5.1 \pm 0.5$
(9) Evel	473	105	2.6	158	0.51	21.101	$0.89 \pm 0.07$	$6.18 \pm 0.22$	$4.5 \pm 0.4$
(9) Evel (c)				158		31.191	$4.62 \pm 0.14$	$2.64 \pm 0.21$	$11.5 \pm 1.3$
(10) Guindy	129	82	1.8	284	0.25	18.734	$0.59 \pm 0.04$	$1.96 \pm 0.13$	$15.7 \pm 1.6$
(11) Isac	681	42	1.5	154	0.42	20.030	$0.52 \pm 0.02$	$1.59 \pm 0.07$	$18.6 \pm 1.7$
(12) Laita	935	152	3.3	315	0.47	17.256	$0.59 \pm 0.05$	$2.15 \pm 0.18$	$15.0 \pm 1.8$
(13) Layon	1057	93	1.7	225	0.39	29.610	$1.61 \pm 0.08$	$3.40 \pm 0.19$	$8.6 \pm 0.9$
(13) Layon				225		31.325	$1.74 \pm 0.07$	$3.51 \pm 0.16$	$8.3 \pm 0.8$
(14) Leff	345	114	1.9	278	0.39	20.072	$0.92 \pm 0.03$	$2.82 \pm 0.11$	$11 \pm 1$

(14) Leff				278		17.809	$0.87 \pm 0.03$	$3.04 \pm 0.12$	$10 \pm 1$
(15) Linon	306	67	1.8	183	0.32	34.370	$3.20 \pm 0.11$	$5.85 \pm 0.24$	$4.6 \pm 0.4$
(16) Meu	764	90	1.9	279	0.34	17.852	$2.29 \pm 0.07$	$7.84 \pm 0.26$	$3.4 \pm 0.3$
(17) Odet	224	145	3.5	305	0.49	17.418	$0.99 \pm 0.06$	$3.44 \pm 0.23$	$9 \pm 1$
(18) Rance aval	894	87	2.0	303	0.27	24.13	$0.66 \pm 0.03$	$1.63 \pm 0.09$	$19.1 \pm 1.9$
(19) Selune	625	166	2.8	308	0.36	33.020	$2.10 \pm 0.16$	$3.95 \pm 0.31$	$7.9 \pm 0.9$
Outcropping bedrocks									
Mont Dol	-	56	-	-	-	26.659	$8.18 \pm 0.14$	$19.27 \pm 0.2.55$	$1.84 \pm 0.18$
Roch'Tre- dudon	-	377	-	-	-	30.534	$4.25 \pm 0.14$	$6.62 \pm 0.6.20$	$5.1 \pm 0.5$
Roch'Tre- dudon	-	369	-	-	-	19.134	$2.04 \pm 0.05$	$8.70 \pm 0.4.34$	$3.8 \pm 0.4$

Name: Watershed or outcrop location name (Fig. 2). All watershed samples are river sands, unless marked (c) for gravel to cobbles sizes. HI: hypsometric integral. Mass Qz: mass of dissolved quartz, weighted at  $10^{-4}$  g precision. The  $^9\text{Be}$  spike mass added was  $150 \pm 2$  mL with a concentration of  $3025 \mu\text{g g}^{-1}$ . Provided ratio are blank corrected (mean of 5 blanks =  $2.21 \pm 0.52 E^{-15}$ . C and  $\sigma_c$ :  $^{10}\text{Be}$  concentration and standard error. d and  $\sigma_d$ : denudation rate and standard error.

$^{10}\text{Be}$  concentrations in three outcrop samples were measured following the same procedure. These three sites (Fig. 4b) are located at the top of locally prominent monadnocks (no topographic mask) and are therefore expected to provide lower-bound erosion rates (i.e., rates mostly controlled by local weathering processes, with little influence of longer wavelength slope-dependent hillslope or fluvial processes).



183

184 Figure 4. Drainage basin data used in the denudation rate model. A) Data from the Octopus drainage basin denudation  
 185 database (Codilean et al., 2018) used for synthetic denudation rate modeling. B) Armorican Massif data from this study.  
 186 Blue dots: sampling locations of drainage basin, with basin number in each polygon (see table 1). Red dots: sampling  
 187 locations of outcrops with estimated denudation rate. Quaternary sedimentation rates around the Armorican Peninsula  
 188 from Augris et al. (2013c, a, b).

189

190 Drainage-basin average denudation rates were derived from  $^{10}\text{Be}$  concentrations using the online CRONUS-  
191 Earth system (Balco et al., 2008) (<https://hess.ess.washington.edu/>). This commonly-used calculator comprises some  
192 simplifications and assumptions that we consider reasonable given our study context: e.g., denudation rates are at  
193 steady-state; river sediments do not have a complex history following first exposure (no significant burial in river  
194 terraces); mean watershed slope and latitude are used for computation of the production rate scaling factor. Given the  
195 regional morphology (small elevation span), the homogeneous climate, and the small size of the sampled watersheds,  
196 we consider that adding more complexity in our denudation rate estimations (e.g., spatial and temporal evolution of  
197 the tree cover) would result in unnecessary questions and uncertainties.

198

### 199 **3.2. Denudation rates**

200 The denudation rates measured in the 19 drainage basins of the Armorican Massif (Table 1) vary between 3  
201 and 27  $\text{m.Ma}^{-1}$ , for an average rate of  $10 \pm 6 \text{ m.Ma}^{-1}$  (mean  $\pm$  standard deviation). Assuming a sea-level high-latitude  
202  $^{10}\text{Be}$  production rate of  $4.11 \pm 0.19 \text{ at.g}^{-1}.\text{yr}^{-1}$  and the Stone scaling scheme (Stone, 2000), these denudation rates are  
203 associated with an integration time between ca. 20 kyr and 200 kyr (average 45 kyr) (Von Blanckenburg, 2005). Thus,  
204 they are representative of the Late Pleistocene period but are also sensitive to the Late Pleistocene - Holocene climate  
205 transition and its impact on denudation rates (e.g., Schaller et al., 2002). Because of the integration times, we consider  
206 that our rates are mostly indicative of Late Pleistocene average conditions, with only the fastest denudation rates ( $> 30$   
207  $\text{m.Ma}^{-1}$ ) potentially biased by the Holocene climate warming.

208 Individual measurement uncertainties are ca. 1–2  $\text{m.Ma}^{-1}$ . For the three sand samples repeated on the same  
209 spot, the denudation rates vary by 0.4–2.5  $\text{m.Ma}^{-1}$ . Differences for the Layon and the Leff rivers are within their  
210 respective uncertainties. The two measurements of the Argenton site shows a 3.6  $\text{m.Ma}^{-1}$  discrepancy. This value is  
211 outside of the individual measurement uncertainties even at the 99% confidence level. Among the possible  
212 explanations, contamination by anthropogenic activity and sediment of artificial low concentrations cannot be  
213 excluded. In any case, the Argenton results remain within the general low erosion rate pattern. The sand / coarser  
214 sample comparison for the Erdre, Douffine, and Evel yields larger differences of 3–20  $\text{m.Ma}^{-1}$ , the largest differences  
215 being associated with a sand denudation rate with a large uncertainty (Douffine,  $\sigma = 5 \text{ m.Ma}^{-1}$ ). Differences in the  
216 sand / sand comparisons have no clear explanation and may simply reflect the internal variability of the erosion and  
217 sediment transport system. This grain-size effect is studied in other places (e.g. Carretier et al., 2009; van Dongen et  
218 al., 2019) but given the relatively small erosion rate difference and mostly because of the small data size we prefer not  
219 to go more into dedicated explanation. This justifies using large-scale database to filter out such variability when  
220 deriving erosion laws (cf., Section 4.1). Hereafter, the denudation rate used for sites with sand / sand or sand / coarser  
221 samples is the average of both measurements.

222 The three outcropping bedrocks show an average erosion rate of  $3.6 \pm 1.8 \text{ m.Ma}^{-1}$ , roughly a third of the  
223 average denudation rate measured in the watersheds. This low value agrees with the expected erosion behavior for  
224 ridges and residuals reliefs (e.g., Dirks et al., 2016) and provides a lower bound for the local long-term erosion rate.

225

## 226 **4. Regional models of denudation and sedimentation rates**

In order to assess the amplitudes and spatial variations of uplift rates due to isostatic response to surface unloading and loading processes, we construct a set of regional models of erosion and sedimentation rates that cover the whole Armorican Massif and neighboring areas up to a few hundred kilometers.

#### 4.1. Denudation rate models

Denudation rates at the watershed scale (over 100 km<sup>2</sup>) are controlled by a combination of the drainage basin morphology (e.g., slope, curvature), its lithology (e.g., soil cover, bedrock nature), its hydrology and dynamics (e.g., runoff, drainage migration), and its local climate (e.g., temperature, precipitation). Several global studies have attempted to define relationships between measured denudation rates and various combinations of statistically predictive parameters (Harrison, 2000; Summerfield and Hulton, 1994; Von Blanckenburg, 2005; Portenga and Bierman, 2011; Harel et al., 2016; Codilean et al., 2018). While their application domains and their results vary, these studies point out that any single parameter or multi-parameter combinations do not predict denudation rates better than within a factor of roughly two or three. All studies also agree that the mean basin slope (or an equivalent proxy) is the most powerful explanatory parameter. However, the relationship between denudation rates and mean slopes breaks down for slope values above 25 – 30°, due to the non-linearity of sediment flux-slope relationship when slopes get closer to stability threshold (Binnie et al., 2007; Montgomery and Brandon, 2002).

In order to build our regional denudation rate models, we analyze denudation rate data for drainage basins from the Octopus database (Codilean et al., 2018) over the non-tectonic areas of Western Europe (Fig. 4a). This database is further filtered to exclude data considered not representative of our study's spatial and temporal scales: We exclude denudation rates higher than 1500 m·Ma<sup>-1</sup> (integration times smaller than a few hundred years), those associated with watershed areas larger than 30,000 km<sup>2</sup> (integration surface too large for regional modeling), and those associated with areas smaller than 100 km<sup>2</sup> (integration surface too sensitive to local transient processes). Our new data from the Armorican Massif complete the Octopus data set by providing information for this up-to-now unsampled low slope region (Fig. 4 and 5). The final dataset comprises 220 denudation rates and morphology parameters, whose correlation is indicated in Table 2. The mean basin slopes and mean basin elevations show the highest correlations with denudation rates, in agreement with global studies. For the Armorican Massif data alone, the correlations are significantly lower, especially for the mean elevation, due to the low spread of denudation rates and morphology parameters.

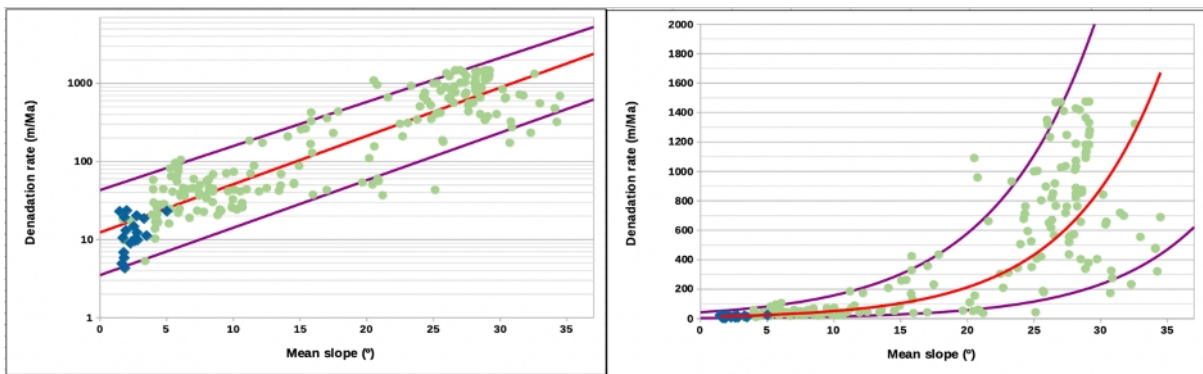


**Figure 5.** Model of denudation rates (m Ma<sup>-1</sup>) vs. mean basin slopes (°). The left and right panels are semi-log and linear representations. Green and blue symbols are from the Octopus database and this study. Best-fit and

minimum/maximum exponential predicting functions are shown in red and purple lines (cf. Text). Typical errors for TCN measurements are of the order of 10 %.

Our regionally-filled erosion models are built using the mean slope parameter on a grid of hexagons with an area of 100 km<sup>2</sup> (roughly the minimal area of our Octopus + Armorican Massif database), i.e., a grid node spacing of ca. 6 km. We do not attempt to fit a process-based relationship for the prediction of erosion; rather, we derive an empirical relationship to produce a continuous erosion map from our isolated observations. The relationship between mean slope ( $s$  in °) and denudation rate ( $d$  in m · Ma<sup>-1</sup>) is based on an exponential function in order to account for the nonlinearity for slope-denudation relation (Fig. 5). The best-fit function ( $d = 12.3 \exp(0.142 s)$ ) is associated with a root-mean-square (RMS) misfit of 22 m · Ma<sup>-1</sup>, strongly controlled by the high denudation rate values (Fig. 5). For the Armorican Massif dataset alone ( $s < 5^\circ$ ), it yields a much smaller RMS misfit of 2 m · Ma<sup>-1</sup>. In order to account for the variability of denudation rates for a given slope value, we estimate two upper- and lower-bound functions that comprise 90% of the data ( $d_{max} = 43 \exp(0.130 s)$  and  $d_{min} = 3.5 \exp(0.140 s)$ ). These two functions are adjusted manually to each exclude 5% of the data over the whole range of denudation rates (Fig. 5).

We use these functions to define two denudation rate models (Fig. 6):

- A mean model based on the best-fit function for all grid cells. Its denudation rates are strongly correlated with the topography and altitude on a regional scale (ca. 100 km), with relatively high rates ca. 15–25 m · Ma<sup>-1</sup> in the high-altitude zones of western Brittany and northeastern Brittany-southern Cotentin, and the lowest rates ca. 5–15 m · Ma<sup>-1</sup> in the low-altitude central region.
- A random model in which each grid cell is associated with a denudation rate based randomly on the lower-bound, best-fit, or upper-bound function. This alternative model will be used to test the sensibility and potential biases of the predicted uplift rates (cf. Section 5). This model results in an average denudation rate larger than that of the mean model by a factor of 1.6, due to the asymmetry of the upper- and lower-bound functions relative to the best-fit one (i.e., the average of the  $d_{min}$  and  $d_{max}$  functions is 1.5 times larger than the best-fit function for the whole slope range). The random model is not correlated with topography and comprises areas of concentrations of high (50–70 m · Ma<sup>-1</sup>) and low (3–7 m · Ma<sup>-1</sup>) denudation rates over distances of 30 – 50 km interspersed between a smaller wavelength random distribution (ca. 10 km, about the grid node spacing).

	Area	Elevation		Slope		HI	Area < 1°
		mean	$\sigma$	mean	$\sigma$		
<b>Armorican Massif</b>	- 0.27	0.25	0.42	0.51	0.48	-0.06	-0.27
<b>Octopus + AM</b>	- 0.23	0.82	0.72	0.76	0.75	0.40	-0.40

Table 2: Denudation rate correlations with basin morphology parameters : Correlation as Pearson coefficient of correlation. For elevation and slope, correlations are given for the mean and the standard deviation ( $\sigma$ ) of the distribution. HI: hypsometric integral. Area < 1°: percentage of basin area with slope lower than 1°. Armorican massif: new data for the Armorican Massif alone. Octopus + AM: final dataset including filtered Octopus and Armorican massif data (cf. text).

#### 4.2. Sedimentation rates

The Pleistocene – Holocene offshore sedimentation around the Armorican Massif is characterized by two main phases: (1) near-field sedimentation along the present-day coastline during the sea-level highstands (interglacial periods) and (2) far-field sedimentation on the continental slope and rise during the sea-level lowstands (glacial periods).

The first phase corresponds to limited terrigenous sedimentation on the continental shelf, primarily at the outlet of the local rivers. Sediment types and thicknesses have been mapped using a marine geophysical and coring surveys (Augris et al., 2013a, b, c), indicating a Quaternary cover of a few meters, up to a few tens of meters in some very localized pockets at the main river mouths (Fig. 4). The English Channel (Manche) is a clear exception to this general pattern, with Quaternary sediment thicknesses up to ca. 50 m localized in the channel of the paleo Manche river. These deposits are not dated but are assumed to be the accumulation of Quaternary highstand sedimentation owing to their geological and geophysical signature (L. Simplet, pers. comm.). These 1–5 m sediment thicknesses correspond to an average sedimentation rate of ca.  $0.5\text{--}2.5\text{ m}\cdot\text{Ma}^{-1}$  over the last 2.5 Ma, with peaks up to  $10\text{--}20\text{ m}\cdot\text{Ma}^{-1}$  in the localized high-sedimentation zones. These sedimentation rates are either too low (one order of magnitude smaller than land denudation rates) or too localized to produce significant effects on land (subsidence rates of  $0\text{--}2\text{ m}\cdot\text{Ma}^{-1}$ , Fig. 7).

The second phase of sedimentation corresponds to large deposits on the continental slope and rise and the oceanic basin during the Pleistocene lowstands. These large turbidite deposits correspond to the combined discharge of the main northwestern Europe rivers through the “River Manche” during the glaciation periods (Toucanne et al., 2009, 2010). The average sedimentation rates may reach a few tens of  $\text{m}\cdot\text{Ma}^{-1}$  at distances of 150–250 km from the Armorican Peninsula.

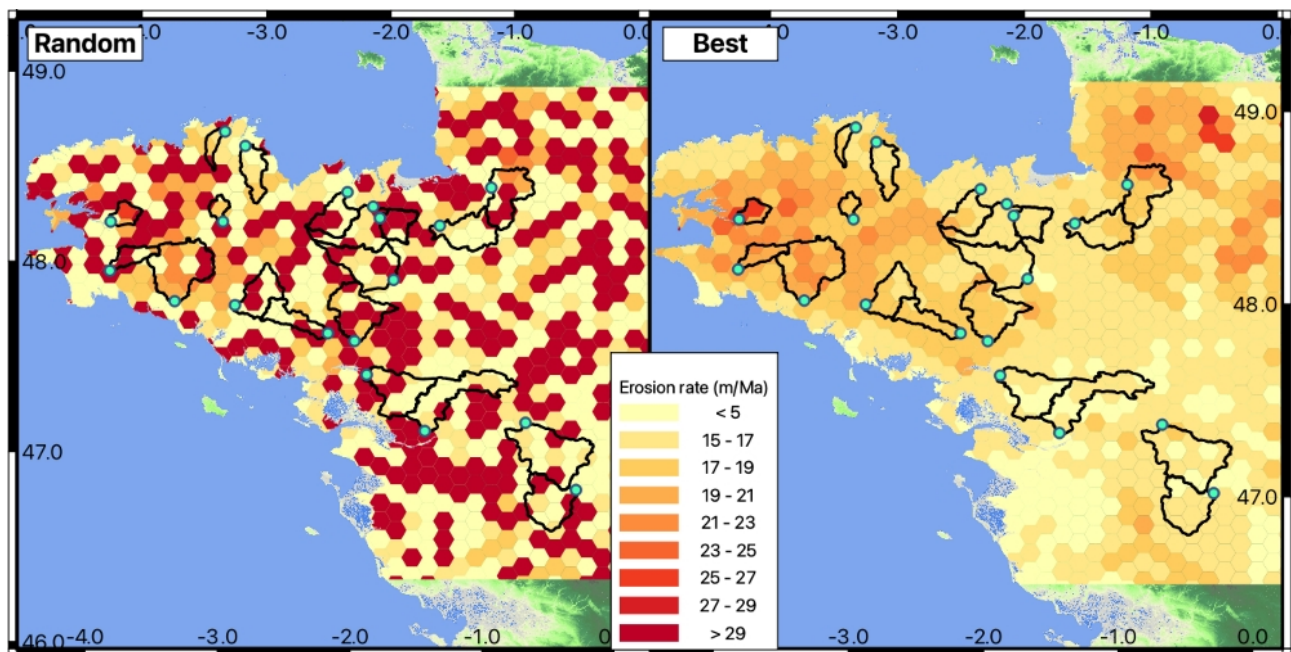


**Figure 6. Best-fit and random denudation rate models.** Denudation rates modeled on  $100\text{ km}^2$  hexagons (6-km grid spacing) using the best-fit (right) and random (left) predictions models (cf. text). Sampled drainage basins and sampling locations are shown by the black outlines and blue dots.

#### 5. Uplift rates driven by surface mass mobilization

## 5.1. Methods

The mechanical response of the lithosphere to surface mass redistribution (erosion or sedimentation) can be modeled with different assumptions, depending primarily on the time scale. For short pulses (days to years), the response can be assumed to followed that of a semi-infinite elastic body (e.g., Steer et al., 2014). At the other end of the spectrum, standard Airy or Pratt isostatic response can be considered over very long time scales of tens of million years (Haxby and Turcotte, 1976). For intermediate time scales of thousands of years to million years, the response to erosion and sedimentation is commonly modeled using a thin elastic plate overlying a low-viscosity fluid (Champagnac et al., 2007; Stephenson and Lambeck, 1985) or using more complex elasto-visco-plastic rheologies (Vernant et al., 2013; Mazzotti et al., 2023). For domains with standard or low continental geotherm or strong rheology, the response of an elasto-visco-plastic lithosphere is close to that of an elastic plate, whereas it may differ significantly in domains with high geotherm or weak rheology (Mazzotti et al., 2023). Here we model the vertical deformation due to Late Pleistocene – Holocene erosion and sedimentation rates following the common assumption of a thin elastic plate, representing the flexural rigidity of the lithosphere. We use two approaches under this assumption, the first following a 3D formalism to study the effect of onshore erosion rates, the second based on a simpler 2D approach to test the impact of offshore sedimentation rates.

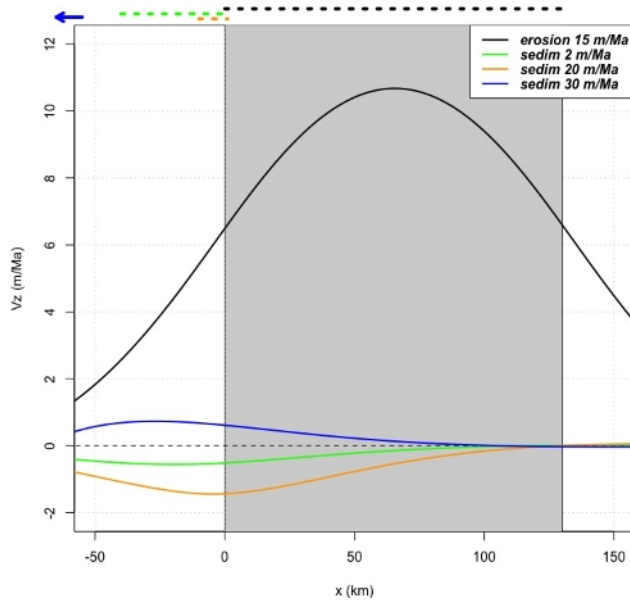
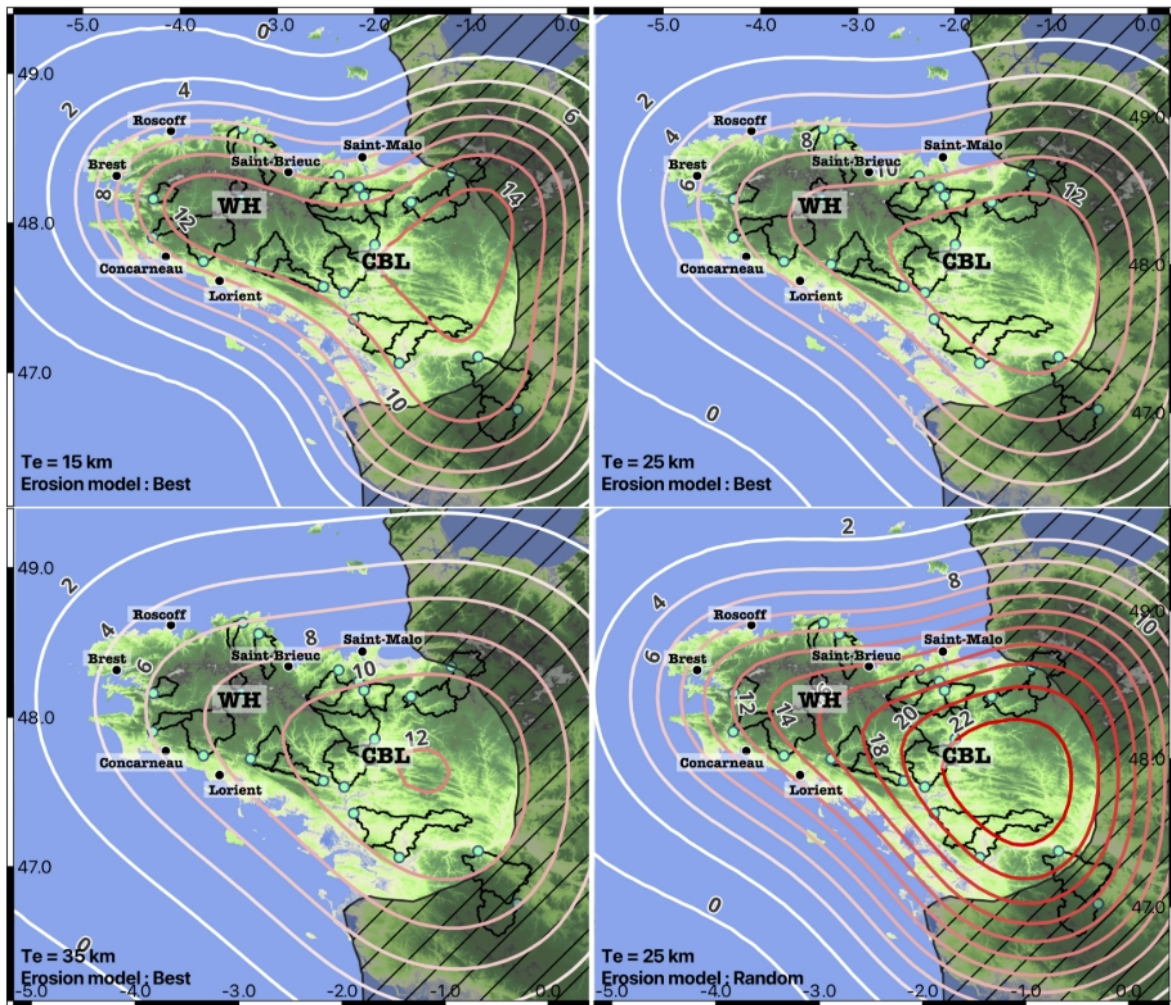


Figure 7. Schematic 2D models of uplift rates due to on-land erosion rates and offshore sedimentation rates. Uplift rates ( $V_z$ ) shown as a function of distance ( $x$ ) along a schematic 2D South-North profile across the Armorican Peninsula, with the gray area indicating the land section. The black curve shows uplift rates due on-land erosion rate of  $15 \text{ m.Ma}^{-1}$  ( $0 \leq x \leq 125 \text{ km}$ ). The green, orange, and blue curves show uplift rates due to three sedimentation rate scenarios:  $2 \text{ m.Ma}^{-1}$  on a 40 km-wide coastal section ( $-40 \leq x \leq 0 \text{ km}$ ),  $20 \text{ m.Ma}^{-1}$  on a 10 km-wide coastal section ( $-10 \leq x \leq 0 \text{ km}$ ),  $30 \text{ m.Ma}^{-1}$  on a 100 km-wide continental slope section ( $-270 \leq x \leq -170 \text{ km}$ ). Uplift rates are given for an elastic plate thickness of 25 km (cf. Section 5). Dashed lines above the graph show locations of the erosion / sedimentation zones.

The response to erosion rates is computed using gFlex (Wickert, 2016) in analytic mode and with default boundary conditions to produce maps of vertical velocities for our two denudation rate models coupled with a range of elastic plate thicknesses derived from rheology and from gravity-topography coherence analyses over Western Europe (Tesauro et al., 2009; Kaban et al., 2018). For the Armorican Massif and neighboring regions, these studies indicate elastic plate thicknesses varying between ca. 15–20 km and ca. 35–40 km. Lateral variations are poorly

351 constrained and show either an eastward increase (Kaban et al., 2018) or small decrease (Tesauro et al., 2009). Thus,  
 352 we test three cases of uniform elastic thicknesses of 15, 25, and 35 km to cover the observed range. Additional model  
 353 parameters include the **plate elastic rigidity** (10 GPa) and Poisson ratio (0.25), and the crust and mantle densities (2700  
 354 and 3200 kg.m<sup>3</sup>, respectively). The spatial extent of our denudation rate models (Fig. 6) is limited to the north by the  
 355 Cotentin Peninsula (not included) and to the east and south by the presence of the Paris and Aquitaine sedimentary  
 356 basins (not included). Based on the response pattern of a 25-km-thick elastic plate, we consider that the predicted  
 357 uplift rates are valid up to ca. 50 km of the model eastern border and are thus limited to the Armorican Peninsula and  
 358 the central Brittany lowland (Fig. 8).



360 Figure 8. Predicted Late Pleistocene - Holocene uplift rates due to denudation rates. Isocontours of uplift rates in m.Ma<sup>-1</sup>. A, B, C: Best-fit erosion model and three elastic plate thicknesses (15, 25, 35 km). D: Random erosion model and 25  
 361 km elastic plate thickness. The grey dashed area on the east side shows where uplift rates are biased by model border  
 362 effects and must not to be considered. CBL and WH stands for Central Brittany Lowland and Western Highland  
 363 respectively.  
 364

365  
 366 The sedimentation impact is tested using on the 2D solution for an infinite elastic plate subjected to a  
 367 punctual load (Turcotte and Schubert, 2014). This 2D model uses a Te value of 25 km and is associated with three  
 368 sedimentation profiles, each representatives of given sedimentation patterns and periods: (1) A coastal sedimentation  
 369 rate of 20 m Ma<sup>-1</sup> extending 10 km offshore from the coast, as an estimation of the maximum current sedimentation.

370 (2) A continental shelf sedimentation rate of  $2 \text{ m Ma}^{-1}$ , from the coast to 40 km offshore, representative of the mean  
371 Quaternary highstand sedimentation. (3) A continental slope sedimentation rate of  $30 \text{ m Ma}^{-1}$  localized 170 to 270 km  
372 offshore, representatives of the Quaternary lowstand sedimentation. These sedimentation models are compared with  
373 an onshore erosion rate of  $15 \text{ m Ma}^{-1}$  extending 125 km from the coast.

374 A primary assumption of both 2D and 3D models is that erosion and sedimentation rates are considered to be  
375 at steady state, thus generating an elastic (time independent) response of the lithosphere. This simplification does not  
376 allow taking into account temporal variations of erosion or sedimentation on time scales of  $10^3$ – $10^4$  years, such as  
377 those associated with climate changes during glacial / interglacial transitions. These transient effects would generate a  
378 response similar to that of classical postglacial rebound processes, mainly depending on the upper mantle effective  
379 viscosity structure (e.g., Peltier, 2022). However, both data and modeling framework are lacking at this stage to  
380 integrate these type of variations in our study.

381  
382

## 383 5.2 Effect of offshore sedimentation

384 Based on the 2D model, we estimate that the effect of offshore sedimentation patterns on vertical velocities  
385 on land is ca.  $0.5$ – $1 \text{ m} \cdot \text{Ma}^{-1}$  (subsidence rate for near-shore sedimentation or uplift rate for slope sedimentation),  
386 about ten times smaller than the effect of denudation rates (Fig. 7). Due to this very low effects of the sedimentation  
387 rates on land vertical motions and to the sparse distribution of sediment thickness mapping, we do not include the  
388 sedimentation rates in the following models. Depending on the interaction of the sedimentation patterns, this could  
389 lead to a small overestimation of ca. 5–15 % of the uplift rates along the coast and less than 5% further inland (Fig. 7).  
390 This effect should be kept in mind when discussing specific model predictions along the coast.

391

## 392 5.3. Effect of onshore erosion

393 Figure 8 (A, B, C) shows the uplift rates predicted for the mean denudation rate model associated with the  
394 three elastic thickness cases. All three models show maximum uplift rates ca.  $12$ – $15 \text{ m} \cdot \text{Ma}^{-1}$  centered on the central  
395 Brittany lowland. The uplift rates decrease westward down to  $4$ – $10 \text{ m} \cdot \text{Ma}^{-1}$  in the Armorican Peninsula, with a  
396 decrease gradient controlled by the elastic plate thickness (lower gradient for thicker plate). This pattern is simply  
397 explained by the fact that uplift rates in central Brittany are due to the combined effects of erosion rates in all  
398 directions, whereas uplift rates in the Armorican Peninsula are only due to erosion rates in the peninsula itself, thus  
399 producing a smaller combined effect. Uplift rates along the Armorican Peninsula coastline are ca.  $8 \text{ m} \cdot \text{Ma}^{-1}$  in the  
400 northeast (Saint-Malo, Saint-Brieuc) and southeast (Lorient, Saint-Nazaire) regions. They diminish to  $4$ – $6 \text{ m} \cdot \text{Ma}^{-1}$  along  
401 the western tip of the peninsula (Roscoff, Brest, Concarneau). The smallest plate-thickness model ( $T_e = 15 \text{ km}$ ) shows a  
402 characteristic elongated pattern of uplift rate ca.  $10$ – $13 \text{ m} \cdot \text{Ma}^{-1}$  along the peninsula east-west axis. This pattern  
403 progressively disappears in the thicker plate models ( $T_e = 25 \text{ km}$  and  $T_e = 35 \text{ km}$ ) due to the low-pass filtering effect of  
404 the elastic plate response that smooths out the erosion rate spatial distribution.

405 The random model allows us to test two effects: (1) the sensibility of the predicted uplift rates to the spatial  
406 distribution of denudation rates, and (2) the possible bias of uplift rates due to the nonlinear slope-denudation rate  
407 relationship. Figure 8D shows an example of uplift rates associated with a random denudation rate distribution (Fig.

6A) for a plate thickness  $T_e = 25$  km. The uplift rate pattern is similar in shape to that of the mean model, albeit with rates ca. 1.5–1.7 times larger depending on the locations along the peninsula due to the denudation rates being on average 1.6 times larger than those of the mean model (cf. Section 4). This model illustrates two important points:

- Spatial variations in denudation rates at dimensions of 10–50 km are filtered out by the flexural rigidity of the lithosphere and are not reflected in the uplift rates. This corresponds to a minimum sensitivity length that varies with the elastic plate thickness but in our case ( $T_e = 15$ –35 km) remains ca. 50 km.
- Considering the uncertainties in denudation rates and the 90% envelop derived from our analysis of stable Western Europe data (Section 4), the random model results provide an upper bound for predicted uplift rates at any given point on the map (but not on average).

## 6. Discussion

### 6.1. Regional denudation and erosion rate variability

Despite the uncertainties on individual denudation rate estimations, we can rely on local and regional averages to identify significant spatial variations. The main signal in the Armorican Massif is the difference between the western highland and central lowland regions. The eight drainage basins fully or primarily eroding the western highland region (Blavet, Claie, Douffine, Evel, Laita, Leff, Odet, and Guindy) show an average denudation rate of  $13 \pm 6$  m.Ma<sup>-1</sup>. In contrast, the nine basins eroding the central lowland (Aff, Argenton, Couesnon, Erdre, Isac, Layon, Linon, Meu, Selune) show an average rate of  $7 \pm 4$  m.Ma<sup>-1</sup>. No other geographical pattern, such as a north-south difference, can be identified. Although its statistical power is low, the difference of factor of 2 in denudation rates between the western highlands and the central lowlands can easily be explained by the small difference in elevation and in relief between the two areas. This result is in good agreement with Bonnet et al. (1998) and Lague et al. (2000) who proposed higher incision and erosion rates by a factor of about 1.5–2 in the western highland compared to the central lowland based on quantitative morphological analyses of the topography.

This spatial variability is also consistent with the estimations of the mean annual sediment export of rivers in these two areas (Delmas et al., 2012). The average export of rivers primarily associated with the western highland is ca. 0.17 Mt.yr<sup>-1</sup>, about twice as large as that of the Vilaine River located in the central lowland (ca. 0.07 Mt.yr<sup>-1</sup>). Considering the respective areas of these two drainage systems, and assuming a sediment density of 1400 kg.m<sup>-3</sup>, the equivalent erosion rates of the western and central regions are ca. 10 and 5 m.Ma<sup>-1</sup>, about 60% of our average denudation rates. Such a difference is commonly observed in studies comparing cosmogenic denudation rates with sediment fluxes (e.g., Kirchner et al., 2001), due possibly to the different sampling time scales of the two methods or to the fact that denudation rates sample both chemical and mechanical erosion processes while suspended sediment flux data lack the dissolved load.

### 6.2. Late Pleistocene – Holocene uplift rates, regional sea level, and geodynamics

Based on present-day elevations of MIS 11 and MIS 5e marine terraces, Pedoja et al. (2018) estimate mean Middle Pleistocene and Upper Pleistocene apparent uplift rates of  $50 \pm 10$  m.Ma<sup>-1</sup> for most of Western Europe coastline, from southern England to Portugal. Using morpho-stratigraphic evidence, they argue that these data cannot

445 be explain solely by eustatic sea-level variations and require a mean uplift rate of ca. 10 m.Ma<sup>-1</sup>, due to an “increasing  
446 lithospheric compression that accompanies Cenozoic orogenies”.

447         Around the Armorican Peninsula, elevated marine terraces of MIS 5e age are found at an average elevation of  
448 6 ± 2 m (full range 4–14 m, data from Pedoja et al. (2018) compilation). Glacial isostatic adjustment corrections and  
449 fingerprinting effects of past icesheets render the estimation of regional Late Pleistocene sea levels particularly difficult  
450 (Hay et al., 2014). Relative to present-day sea level, MIS 5e eustatic elevations are estimated ca. 2–9 m at 123–125 ka  
451 (with preferred value of 4.5–7.5 m) and ca. -20 m at 113 ka, with a likely intermediate highstand ca. 5 m at 116–188 ka  
452 (Kopp et al., 2013; Polyak et al., 2018; Hay et al., 2014). Assuming a regional eustatic sea level of 2, 4.5, 7.5, or 9 m  
453 results in a **Late Pleistocene uplift rate** of -23, -12, 12, or 31 m.Ma<sup>-1</sup>, respectively, for the Armorican Peninsula marine  
454 terrace (average elevation of 6 m). In comparison, we estimate uplift rates of 4–8 m.Ma<sup>-1</sup> (upper bound of 6–14 m.Ma<sup>-1</sup>  
455 <sup>1</sup>) due to the response to denudation rates (Fig. 8).

456         Thus, within the uncertainties associated with the different sea level estimations, erosion-driven uplift can  
457 explain the uplifted Upper Pleistocene marine terraces around the Armorican Peninsula, without a need for an  
458 additional geodynamic process. Another way to consider these results is that, if denudation alone drives the uplift of  
459 the Armorican Peninsula coastline, the elevation of the marine terraces constrains the regional Upper Pleistocene sea  
460 level to a highstand ca. 5 m. A **third interpretation is that additional uplift due to other geodynamic processes (in**  
461 **addition to erosion) would require a low regional eustatic sea level (2–5 m).**

462

### 463 **6.3. Quaternary morphology and tectonics**

464         The elevations of marine deposits, corrected for past eustatic sea level, provide first-order estimations of  
465 Quaternary uplift rates in the central lowland region of the Armorican Massif (Section 2). They indicate an average  
466 uplift rate of 4–13 m·Ma<sup>-1</sup> since ca. 3 Ma (Brault et al., 2004) or 16 ± 2 m·Ma<sup>-1</sup> average during the Pleistocene (Bessin  
467 et al., 2017). If we assume that our denudation rates are representative of the Quaternary period (mix of glacial and  
468 interglacial periods), these geological uplift rates are in good agreement with those predicted in response to erosion  
469 (ca. 12–15 m.Ma<sup>-1</sup>, upper bound ca. 20 m.Ma<sup>-1</sup>, Fig. 8). As for the Upper Pleistocene marine terraces, this comparison  
470 suggests that erosion-driven uplift is enough to explain the elevated Quaternary marine markers.

471         The pattern of uplift rates due to denudation rates also points out a minor difference between the western  
472 highland (ca. 6–12 m.Ma<sup>-1</sup>) and the central lowland (ca. 12–15 m.Ma<sup>-1</sup>), depending on the **assumed lithosphere flexural**  
473 **rigidity** (Fig. 8). Combined with the opposite pattern of denudation rates (ca. 20 and 15 m.Ma<sup>-1</sup> in the western and  
474 central regions, respectively, Fig. 6), these results suggest a quasi-stationary surface elevation in the central lowland  
475 whereas the absolute elevation of the western highland region diminishes by ca. 10 m.Ma<sup>-1</sup>. These very low rates of  
476 topographic evolution indicate a persistence of the present-day east-west elevation differences throughout the  
477 Quaternary, despite the Mid Pleistocene reconfiguration of the drainage network (Guillocheau et al., 2003; Brault et  
478 al., 2004).

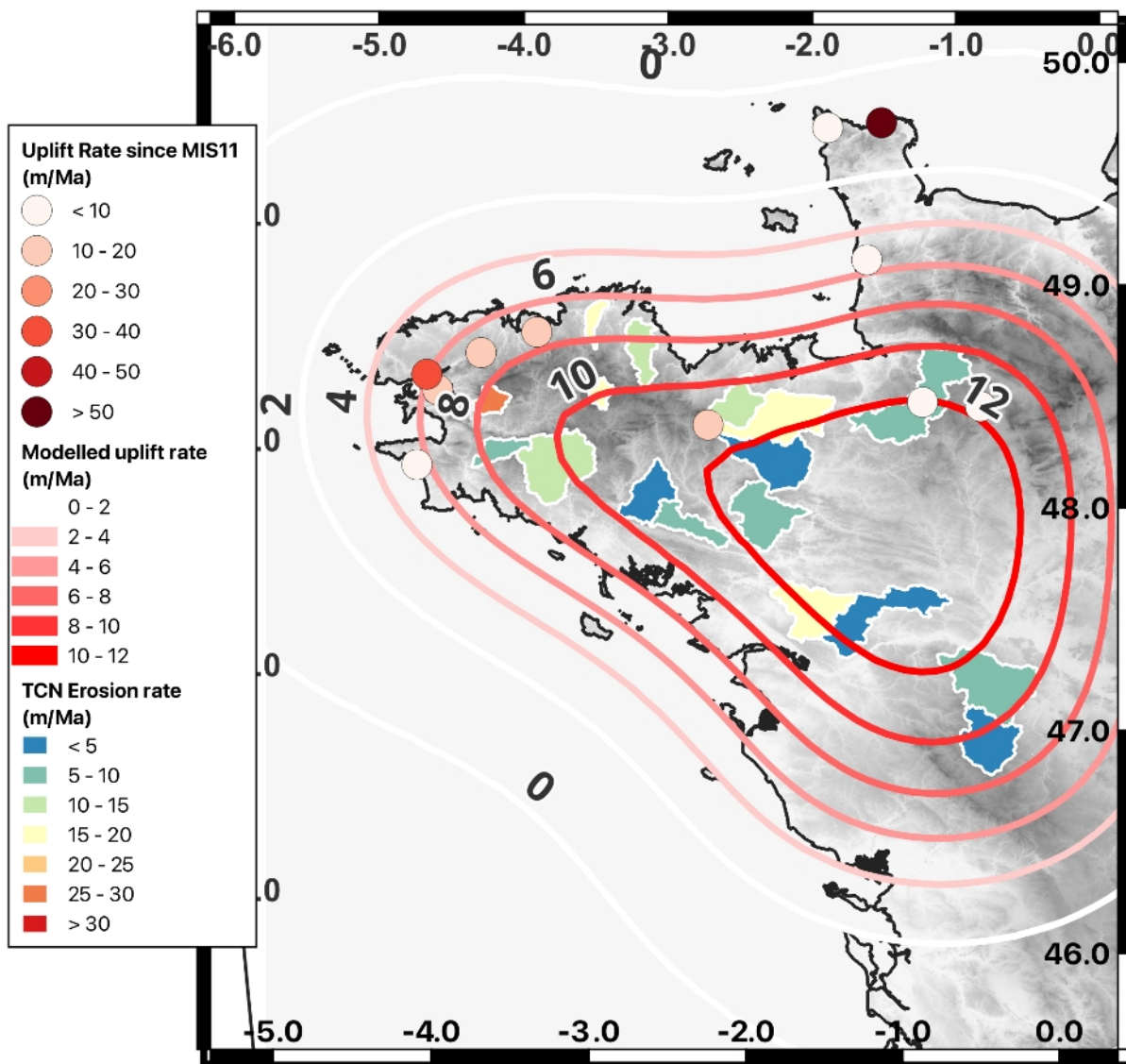


Figure 9: Summary of the measured denudation rate, derived uplift rate due to erosional isostatic adjustment and observed uplifted marine terraces (from Pedoja et al., 2018). The flexural response to erosion is provided for a  $T_e = 25$  km and the best synthetic erosional model.

Finally, our results do not support the differential uplift rates across the QNEF system, accommodating 10–60  $\text{m} \cdot \text{Ma}^{-1}$  of east-side-down relative vertical motion, proposed by Bonnet et al. (1998) and Lague et al. (2000). If erosion alone drives Quaternary uplift, as suggested by the agreement with the Cenozoic marine deposits, then the differential western / central uplift rates is less than a few  $\text{m} \cdot \text{Ma}^{-1}$  and in the opposite direction (east-side up, Fig. 8 and 9). Additional processes such as local tectonics could induce the proposed differential uplift rates and QNEF system motion. However, this would result in differential altitudes of ca. 1.5–8 m of the MIS 5e marine terraces on both sides of the QNEF system along the northern Armorican Peninsula coast. The variability in the local terrace data preclude a robust conclusion, but they do not show a clear east-west difference in altitudes (Fig. 9). An alternative explanation is to consider that the east-west difference in incision rates observed by Bonnet et al. (1998) and Lague et al. (2000) is not due to a difference in uplift rates, but to a difference in the erosion state of the western highland and central lowland: In the latter, the low relief and relatively high erodibility of the Faluns Sea sediment deposits may have resulted in fast erosion processes post 2 Ma, and thus present-day low erosion and incision rates associated with a

smooth landscape. In contrast, the western highland was characterized by higher relief and lower (bedrock) erodibility ca. 2 Ma, and thus may still currently be in a transient state of higher erosion and incision rates.

Overall, the lack of marine deposits in the western highland and the variability in the marine terrace data preclude distinguishing between the two propositions and the potential activity, or not, of the QNEF system.

500

## 501 **7. Conclusion**

In the Armorican Massif, denudation rates measured from terrestrial cosmogenic nuclide concentrations range between 3 and 27 m.Ma<sup>-1</sup>. These rates are representative of the Late Pleistocene (20–200 kyr). On average, the western highland region of the Armorican Massif shows denudation rates about twice those of the central lowland region (13 ± 6 m.Ma<sup>-1</sup> vs. 7 ± 4 m.Ma<sup>-1</sup>, Fig. 9), in general agreement with previous regional morphology and erosion studies (Bonnet et al., 1998; Lague et al., 2000; Delmas et al., 2012). There is no clear denudation signal associated with large-scale tectonic structures (e.g., South-Armorican Shear Zone, Quessnoy-Nort-sur-Erdre Fault).

The lithosphere flexural isostatic response to these ongoing denudation rates results in an overall uplift of the Armorican Peninsula. Predicted uplift rates range from ca. 12–15 m.Ma<sup>-1</sup> in the central lowland region to ca. 4–10 m.Ma<sup>-1</sup> in the western peninsula and ca. 4–8 m.Ma<sup>-1</sup> along the coast (Fig. 9).

Considering the uncertainties in eustatic sea-level corrections, these erosion-driven uplift rates can explain the uplifted Late Pleistocene marine terraces along the Armorican Peninsula coastline (Pedoja et al., 2018), without necessitating additional geodynamic processes such as regional compression or local active faults. While our results do not preclude the existence of such other processes, they show that, if present, their effects must be much slower than previously proposed (Bonnet et al., 1998). Finally, assuming that they can be extrapolated over the whole Pleistocene period, the erosion-driven uplift rates in the central lowland region are also sufficient to explain the elevated Quaternary marine deposits (Brault et al., 2004; Bessin et al., 2017).

Our results show that long-term erosion over the Holocene and Pleistocene can be a major driver of the observed uplift in the Armorican Peninsula and, likely, in other stable continental regions. While other geodynamics processes may also contribute to these uplift rates, spatial variations in erosion rates should be taken into account for before trying to derive global or regional geodynamic or tectonic conclusions (Gurnis et al., 2000; Pedoja et al., 2011; Murray-Wallace et al., 1996; Bonnet et al., 2000). They also suggest that the role of long-term erosion as a driver or promoter of intraplate seismicity should be considered in the Armorican Peninsula and other stable continental regions (Gallen and Thigpen, 2018; Mazzotti et al., 2023).

525

## 526 **Author contributions.**

O. M. and S. M. performed the field work and sampling. O. M. and V. G. performed the sample preparation. O. M. and S. M. performed the initial data analysis and draft of the manuscript. All authors discussed the result, the data analysis and commented on the manuscript.

530

## 531 **Competing interests.**

The contact author has declared that none of the authors has any competing interests.

533

534

## 535 **Acknowledgments**

This study was supported by the French “Agence Nationale de la Recherche”, project ANR-20-CE01-0005 “EroSeis”. Models, data analyses, and figures were done with open-source, free software (<https://www.python.org/>,

538 <https://www.ggis.org/>, <https://github.com/awickert/gFlex>). Model parameters and results are available on demand on  
 539 the Open Science Framework "EroSeis" project (<https://osf.io/yq3bt/>). We thank Laure Simplet (Ifremer) for providing  
 540 the sedimentation databases and information, and Samuel Toucanne (Ifremer) for the Manche river references. The  
 541 <sup>10</sup>Be measurements were performed at the ASTER AMS national facility (CEREGE, Aix en Provence) which is supported  
 542 by the INSU/CNRS, the ANR through the "Projets thématiques d'excellence" program for the "Equipements  
 543 d'excellence" ASTER-CEREGE action and IRD.

544

## 545 Bibliography

- 546 Arnold, M., Merchel, S., Bourlès, D. L., Braucher, R., Benedetti, L., Finkel, R. C., Aumaître, G., Gott dang, A., and Klein,  
 547 M.: The French accelerator mass spectrometry facility ASTER: Improved performance and developments, Nucl.  
 548 Instrum. Methods Phys. Res. Sect. B Beam Interact. Mater. At., 268, 1954–1959,  
 549 <https://doi.org/10.1016/j.nimb.2010.02.107>, 2010.
- 550 Augris, C., Simplet, L., and Gautier, E.: Isopaques de bancs sableux en Mer du Nord, Manche et Atlantique,  
 551 <https://doi.org/10.12770/75AD486F-9D03-4FEB-B742-BE6C6F791345>, 2013a.
- 552 Augris, C., Simplet, L., and Gautier, E.: Isopaques de couverture indifférenciée en Mer du Nord, Manche et Atlantique,  
 553 <https://doi.org/10.12770/C841CA37-B414-4C51-AD6A-16BC34E8CF6F>, 2013b.
- 554 Augris, C., Simplet, L., and Gautier, E.: Isopaques de nappes alluviales en Mer du Nord, Manche et Atlantique,  
 555 <https://doi.org/10.12770/6C4CCD44-71B1-411D-91D1-ECCD1B2A46F1>, 2013c.
- 556 Balco, G., Stone, J. O., Lifton, N. A., and Dunai, T. J.: A complete and easily accessible means of calculating surface  
 557 exposure ages or erosion rates from <sup>10</sup>Be and <sup>26</sup>Al measurements, Quat. Geochronol., 3, 174–195,  
 558 <https://doi.org/10.1016/j.quageo.2007.12.001>, 2008.
- 559 Ballèvre, M., Bosse, V., Ducassou, C., and Pitra, P.: Palaeozoic history of the Armorican Massif: Models for the tectonic  
 560 evolution of the suture zones, Comptes Rendus Geosci., 341, 174–201, <https://doi.org/10.1016/j.crte.2008.11.009>,  
 561 2009.
- 562 Bessin, P., Guillocheau, F., Robin, C., Schroëtter, J.-M., and Bauer, H.: Planation surfaces of the Armorican Massif  
 563 (western France): Denudation chronology of a Mesozoic land surface twice exhumed in response to relative crustal  
 564 movements between Iberia and Eurasia, Geomorphology, 233, 75–91,  
 565 <https://doi.org/10.1016/j.geomorph.2014.09.026>, 2014.
- 566 Bessin, P., Guillocheau, F., Robin, C., Braun, J., Bauer, H., and Schroëtter, J.-M.: Quantification of vertical movement of  
 567 low elevation topography combining a new compilation of global sea-level curves and scattered marine deposits  
 568 (Armorican Massif, western France), Earth Planet. Sci. Lett., 470, 25–36, <https://doi.org/10.1016/j.epsl.2017.04.018>,  
 569 2017.
- 570 Beucler, É., Bonnin, M., Hourcade, C., Van Vliet-Lanoë, B., Perrin, C., Provost, L., Mocquet, A., Battaglia, J., Geoffroy, L.,  
 571 Steer, P., Le Gall, B., Douchain, J.-M., Fligiel, D., Gernigon, P., Delouis, B., Perrot, J., Mazzotti, S., Mazet-Roux, G.,  
 572 Lambotte, S., Grunberg, M., Vergne, J., Clément, C., Calais, É., Deverchère, J., Longuevergne, L., Duperret, A., Roques,  
 573 C., Kaci, T., and Authemayou, C.: Characteristics and possible origins of the seismicity in northwestern France, Comptes  
 574 Rendus Géoscience, 353, 53–77, <https://doi.org/10.5802/crgeos.86>, 2021.
- 575 Binnie, S. A., Phillips, W. M., Summerfield, M. A., and Fifield, L. K.: Tectonic uplift, threshold hillslopes, and denudation  
 576 rates in a developing mountain range, Geology, 35, 743, <https://doi.org/10.1130/G23641A.1>, 2007.
- 577 Bonnet, S., Guillocheau, F., and Brun, J.-P.: Relative uplift measurement using river incisions: the case of the Armorican  
 578 basement (France), Comptes Rendus Académie Sci. - Earth Planet. Sci., 327, 245–251, 1998.

579 Bonnet, S., Guillocheau, F., Brun, J.-P., and Van Den Driessche, J.: Large-scale relief development related to Quaternary  
580 tectonic uplift of a Proterozoic-Paleozoic basement: The Armorican Massif, NW France, *J. Geophys. Res. Solid Earth*,  
581 105, 19273–19288, <https://doi.org/10.1029/2000JB900142>, 2000.

582 Braucher, R., Guillou, V., Bourlès, D. L., Arnold, M., Aumaître, G., Keddadouche, K., and Nottoli, E.: Preparation of ASTER  
583 in-house  $^{10}\text{Be}/^{9}\text{Be}$  standard solutions, *Nucl. Instrum. Methods Phys. Res. Sect. B Beam Interact. Mater. At.*, 361, 335–  
584 340, <https://doi.org/10.1016/j.nimb.2015.06.012>, 2015.

585 Brault, N., Bourquin, S., Guillocheau, F., Dabard, M.-P., Bonnet, S., Courville, P., Estéoule-Choux, J., and Stepanoff, F.:  
586 Mio-Pliocene to Pleistocene paleotopographic evolution of Brittany (France) from a sequence stratigraphic analysis:  
587 relative influence of tectonics and climate, *Sediment. Geol.*, 163, 175–210, [https://doi.org/10.1016/S0037-](https://doi.org/10.1016/S0037-0738(03)00193-3)  
588 0738(03)00193-3, 2004.

589 Carretier, S., Regard, V., & Soual, C. (2009). Theoretical cosmogenic nuclide concentration in river bed load clasts: Does  
590 it depend on clast size?. *Quaternary Geochronology*, 4(2), 108–123.

591 Champagnac, J.-D., Molnar, P., Anderson, R. S., Sue, C., and Delacou, B.: Quaternary erosion-induced isostatic rebound  
592 in the western Alps, *Geology*, 35, 195–198, <https://doi.org/10.1130/G23053A.1>, 2007.

593 Codilean, A. T., Munack, H., Cohen, T. J., Saktura, W., Gray, A. G., and Mudd, S. M.: OCTOPUS: An open cosmogenic  
594 isotope and luminescence database, *Earth Syst. Sci. Data*, 10, 2123–2139, <https://doi.org/10.5194/essd-10-2123-2018>,  
595 2018.

596 Delmas, M., Cerdan, O., Cheviron, B., Mouchel, J.-M., and Eyrolle, F.: Sediment export from French rivers to the sea,  
597 *Earth Surf. Process. Landf.*, 37, 754–762, <https://doi.org/10.1002/esp.3219>, 2012.

598 Dirks, P. H. G. M., Placzek, C. J., Fink, D., Dosseto, A., and Roberts, E.: Using  $^{10}\text{Be}$  cosmogenic isotopes to estimate  
599 erosion rates and landscape changes during the Plio-Pleistocene in the Cradle of Humankind, South Africa, *J. Hum.*  
600 *Evol.*, 96, 19–34, <https://doi.org/10.1016/j.jhevol.2016.03.002>, 2016.

601 Dutton, A. and Lambeck, K.: Ice Volume and Sea Level During the Last Interglacial, *Science*, 337, 216–219,  
602 <https://doi.org/10.1126/science.1205749>, 2012.

603 Erlanger, E.D., Granger, D.E., and Gibbon, R.J.: Rock uplift rates in South Africa from isochron burial dating of fluvial and  
604 marine terraces, *Geology*, 40, 11, 1019–1022, doi:10.1130/G33172.1.

605  
606 Gallen, S. F. and Thigpen, J. R.: Lithologic Controls on Focused Erosion and Intraplate Earthquakes in the Eastern  
607 Tennessee Seismic Zone, *Geophys. Res. Lett.*, 45, 9569–9578, <https://doi.org/10.1029/2018GL079157>, 2018.

608 Granger, D. E., Kirchner, J. W., & Finkel, R. C. (1996). Spatially Averaged Long-Term Erosion Rates Measured from In Situ-  
609 Produced Cosmogenic Nuclides in Alluvial Sediment. *The Journal of Geology*, 104, 249–257.

610 Guillocheau, F., Brault, Thomas, Barbarand, J., Bonnet, S., Bourquin, S., J, E.-C., Guennoc, P., Menier, D., Néraudeau, D.,  
611 Proust, J.-N., and Wyns, R.: Histoire géologique du Massif Armoricaïn depuis 140 Ma (Crétacé-Actuel), *Assoc.*  
612 *Géologues Bassin Paris*, 40, 13–28, 2003.

613 Gurnis, M., Mitrovica, J. X., Ritsema, J., and van Heijst, H.-J.: Constraining mantle density structure using geological  
614 evidence of surface uplift rates: The case of the African Superplume, *Geochem. Geophys. Geosystems*, 1, n/a-n/a,  
615 <https://doi.org/10.1029/1999GC000035>, 2000.

616 Harel, M.-A., Mudd, S. M., and Attal, M.: Global analysis of the stream power law parameters based on worldwide  
617  $^{10}\text{Be}$  denudation rates, *Geomorphology*, 268, 184–196, <https://doi.org/10.1016/j.geomorph.2016.05.035>, 2016.

618 Harrison, C. G. A.: What factors control mechanical erosion rates?, *Int. J. Earth Sci.*, 88, 752–763,  
619 <https://doi.org/10.1007/s005310050303>, 2000.

620 Haxby, W. F. and Turcotte, D. L.: Stresses induced by the addition or removal of overburden and associated thermal  
621 effects, *Geology*, 4, 181, <https://doi.org/10.1130/0091-7613>, 1976.

622 Hay, C., Mitrovica, J. X., Gomez, N., Creveling, J. R., Austermann, J., and E. Kopp, R.: The sea-level fingerprints of ice-  
623 sheet collapse during interglacial periods, *Quat. Sci. Rev.*, 87, 60–69, <https://doi.org/10.1016/j.quascirev.2013.12.022>,  
624 2014.

625 Kaban, M. K., Chen, B., Tesauero, M., Petrunin, A. G., El Khrepy, S., and Al-Arifi, N.: Reconsidering Effective Elastic  
626 Thickness Estimates by Incorporating the Effect of Sediments: A Case Study for Europe, *Geophys. Res. Lett.*, 45, 9523–  
627 9532, <https://doi.org/10.1029/2018GL079732>, 2018.

628 Kirchner, J. W., Finkel, R. C., Riebe, C. S., Granger, D. E., Clayton, J. L., King, J. G., and Megahan, W. F.: Mountain erosion  
629 over 10 yr, 10 k.y., and 10 m.y. time scales, *Geology*, 29, 591, [https://doi.org/10.1130/0091-  
630 7613\(2001\)029<0591:MEOYKY>2.0.CO;2](https://doi.org/10.1130/0091-7613(2001)029<0591:MEOYKY>2.0.CO;2), 2001.

631 Kopp, R. E., Simons, F. J., Mitrovica, J. X., Maloof, A. C., and Oppenheimer, M.: A probabilistic assessment of sea level  
632 variations within the last interglacial stage, *Geophys. J. Int.*, 193, 711–716, <https://doi.org/10.1093/gji/ggt029>, 2013.

633 Lague, D., Davy, P., and Crave, A.: Estimating uplift rate and erodibility from the area-slope relationship: Examples from  
634 Brittany (France) and numerical modelling, *Phys. Chem. Earth Part Solid Earth Geod.*, 25, 543–548,  
635 [https://doi.org/10.1016/S1464-1895\(00\)00083-1](https://doi.org/10.1016/S1464-1895(00)00083-1), 2000.

636 Lenôtre, N., Thierry, P., Blanchin, R., and Brochard, G.: Current vertical movement demonstrated by comparative  
637 levelling in Brittany (northwestern France), *Tectonophysics*, 301, 333–344, 1999.

638 Masson, C., Mazzotti, S., Vernant, P., and Doerflinger, E.: Extracting small deformation beyond individual station  
639 precision from dense GNSS networks in France and Western Europe, *Solid Earth*, 10, 1905–1920,  
640 <https://doi.org/10.5194/se-10-1905-2019>, 2019.

641 Mazzotti, S., Vergeron, X., Malcles, O., Grosset, J., and Vernant, P.: Impact of long-term erosion on crustal stresses and  
642 seismicity in stable continental regions, *Geology*, 51, 733–737, <https://doi.org/10.1130/G51327.1>, 2023.

643 Monnier Jean Laurent, Jumel Guy, Jumel Alain. Le Paléolithique inférieur de la côte 42 à Saint-Malo-de-Phily (Ille-et-  
644 Vilaine). Stratigraphie et industrie. In: *Bulletin de la Société préhistorique française*, tome 78, n°10-12, 1981. Études et  
645 Travaux. pp. 317-328. DOI : <https://doi.org/10.3406/bspf.1981.5285>

646 Montgomery, D. R. and Brandon, M. T.: Topographic controls on erosion rates in tectonically active mountain ranges,  
647 *Earth Planet. Sci. Lett.*, 201, 481–489, [https://doi.org/10.1016/S0012-821X\(02\)00725-2](https://doi.org/10.1016/S0012-821X(02)00725-2), 2002.

648 Muhs, D. R., Pandolfi, J. M., Simmons, K. R., and Schumann, R. R.: Sea-level history of past interglacial periods from  
649 uranium-series dating of corals, Curaçao, Leeward Antilles islands, *Quat. Res.*, 78, 157–169,  
650 <https://doi.org/10.1016/j.yqres.2012.05.008>, 2012.

651 Murray-Wallace, C. M., Belperio, A. P., Cann, J. H., Huntley, D. J., and Prescott, J. R.: Late Quaternary uplift history,  
652 Mount Gambier Region, South Australia, *Z. Geomorphol., Suppl.-Bd.* 106, 41–56, 1996.

653 Néraudeau, D., Barbe, S., Mercier, D., and Roman, J.: Signatures paléoclimatiques des échinides du Néogène final  
654 atlantique à faciès redonien, *Ann. Paléontol.*, 89, 153–170, [https://doi.org/10.1016/S0753-3969\(03\)00023-5](https://doi.org/10.1016/S0753-3969(03)00023-5), 2003.

655 Pedoja, K., Husson, L., Regard, V., Cobbold, P. R., Ostanciaux, E., Johnson, M. E., Kershaw, S., Saillard, M., Martinod, J.,  
656 Furgerot, L., Weill, P., and Delcaillau, B.: Relative sea-level fall since the last interglacial stage: Are coasts uplifting  
657 worldwide?, *Earth-Sci. Rev.*, 108, 1–15, <https://doi.org/10.1016/j.earscirev.2011.05.002>, 2011.

658 Pedoja, K., Jara-Muñoz, J., De Gelder, G., Robertson, J., Meschis, M., Fernandez-Blanco, D., Nexer, M., Poprawski, Y.,  
659 Dugué, O., Delcaillau, B., Bessin, P., Benabdelouahed, M., Authemayou, C., Husson, L., Regard, V., Menier, D., and Pinel,  
660 B.: Neogene-Quaternary slow coastal uplift of Western Europe through the perspective of sequences of strandlines

661 from the Cotentin Peninsula (Normandy, France), *Geomorphology*, 303, 338–356,  
662 <https://doi.org/10.1016/j.geomorph.2017.11.021>, 2018.

663 Peltier, W.R.: Glacial isostatic adjustment: physical models and observational constraints, *Rep.*  
664 *Prog. Phys.*, 85, 096801, 2022.

665 Polyak, V. J., Onac, B. P., Fornós, J. J., Hay, C., Asmerom, Y., Dorale, J. A., Ginés, J., Tuccimei, P., and Ginés, A.: A highly  
666 resolved record of relative sea level in the western Mediterranean Sea during the last interglacial period, *Nat. Geosci.*,  
667 11, 860–864, <https://doi.org/10.1038/s41561-018-0222-5>, 2018.

669 Portenga, E. W. and Bierman, P. R.: Understanding Earth's eroding surface with  $^{10}\text{Be}$ , *GSA Today*, 21, 4–10,  
670 <https://doi.org/10.1130/G111A.1>, 2011.

671 Raymo, M. E. and Mitrovica, J. X.: Collapse of polar ice sheets during the stage 11 interglacial, *Nature*, 483, 453–456,  
672 <https://doi.org/10.1038/nature10891>, 2012.

673 Ruzsaniczay-Rüdiger, Z., Neuhuber, S., Braucher, R., Lachner, J., Steier, P., Wieser, A., Braun, M., ASTER Team, Bourlès, D.,  
674 Aumaître, G., and Keddadouche, K.: Comparison and performance of two cosmogenic nuclide sample preparation  
675 procedures of in situ produced  $^{10}\text{Be}$  and  $^{26}\text{Al}$ , *J. Radioanal. Nucl. Chem.*, 329, 1523–1536,  
676 <https://doi.org/10.1007/s10967-021-07916-4>, 2021.

677 Schaller, M., Von Blanckenburg, F., Veldkamp, A., Tebbens, L. A., Hovius, N., and Kubik, P. W.: A 30 000 yr record of  
678 erosion rates from cosmogenic  $^{10}\text{Be}$  in Middle European river terraces, *Earth Planet. Sci. Lett.*, 204, 307–320,  
679 [https://doi.org/10.1016/S0012-821X\(02\)00951-2](https://doi.org/10.1016/S0012-821X(02)00951-2), 2002.

680 Siddall, M., Chappell, J., and Potter, E.-K.: Eustatic sea level during past interglacials, in: *Developments in Quaternary*  
681 *Sciences*, vol. 7, Elsevier, 75–92, [https://doi.org/10.1016/S1571-0866\(07\)80032-7](https://doi.org/10.1016/S1571-0866(07)80032-7), 2007.

682 Steer, P., Simoes, M., Cattin, R., and Shyu, J. B. H.: Erosion influences the seismicity of active thrust faults, *Nat.*  
683 *Commun.*, 5, 5564, <https://doi.org/10.1038/ncomms6564>, 2014.

684 Stephenson, R. and Lambeck, K.: Erosion-isostatic rebound models for uplift: an application to south-eastern Australia,  
685 *Geophys. J. Int.*, 82, 31–55, <https://doi.org/10.1111/j.1365-246X.1985.tb05127.x>, 1985.

686 Stone, J. O.: Air pressure and cosmogenic isotope production, *J. Geophys. Res. Solid Earth*, 105, 23753–23759,  
687 <https://doi.org/10.1029/2000JB900181>, 2000.

688 Summerfield, M. A. and Hulton, N. J.: Natural controls of fluvial denudation rates in major world drainage basins, *J.*  
689 *Geophys. Res. Solid Earth*, 99, 13871–13883, <https://doi.org/10.1029/94JB00715>, 1994.

690 Tesauero, M., Kaban, M. K., and Cloetingh, S. A. P. L.: How rigid is Europe's lithosphere?, *Geophys. Res. Lett.*, 36,  
691 <https://doi.org/10.1029/2009GL039229>, 2009.

692 Toucanne, S., Zaragosi, S., Bourillet, J. F., Cremer, M., Eynaud, F., Van Vliet-Lanoë, B., Penaud, A., Fontanier, C., Turon, J.  
693 L., and Cortijo, E.: Timing of massive 'Fleuve Manche' discharges over the last 350kyr: insights into the European ice-  
694 sheet oscillations and the European drainage network from MIS 10 to 2, *Quat. Sci. Rev.*, 28, 1238–1256,  
695 <https://doi.org/10.1016/j.quascirev.2009.01.006>, 2009.

696 Toucanne, S., Zaragosi, S., Bourillet, J.-F., Marieu, V., Cremer, M., Kageyama, M., Van Vliet-Lanoë, B., Eynaud, F., Turon,  
697 J.-L., and Gibbard, P. L.: The first estimation of Fleuve Manche palaeoriver discharge during the last deglaciation:  
698 Evidence for Fennoscandian ice sheet meltwater flow in the English Channel ca 20–18 ka ago, *Earth Planet. Sci. Lett.*,  
699 290, 459–473, <https://doi.org/10.1016/j.epsl.2009.12.050>, 2010.

700 van Dongen, R., Scherler, D., Wittmann, H., & von Blanckenburg, F. (2019). Cosmogenic  $^{10}\text{Be}$  in river sediment: where  
701 grain size matters and why. *Earth Surface Dynamics*, 7(2), 393–410.

- 702 Vernant, P., Hivert, F., Chéry, J., Steer, P., Cattin, R., and Rigo, A.: Erosion-induced isostatic rebound triggers extension in  
703 low convergent mountain ranges, *Geology*, 41, 467–470, <https://doi.org/10.1130/G33942.1>, 2013.
- 704 Von Blanckenburg, F.: The control mechanisms of erosion and weathering at basin scale from cosmogenic nuclides in  
705 river sediment, *Earth Planet. Sci. Lett.*, 237, 462–479, <https://doi.org/10.1016/j.epsl.2005.06.030>, 2005.
- 706 Westaway, R., Maddy, D., and Bridgland, D.: Flow in the lower continental crust as a mechanism for the Quaternary  
707 uplift of south-east England: constraints from the Thames terrace record, *Quat. Sci. Rev.*, 21, 559–603,  
708 [https://doi.org/10.1016/S0277-3791\(01\)00040-3](https://doi.org/10.1016/S0277-3791(01)00040-3), 2002.
- 709 Wickert, A. D.: Open-source modular solutions for flexural isostasy: gFlex v1.0, *Geosci. Model Dev.*, 9, 997–1017,  
710 <https://doi.org/10.5194/gmd-9-997-2016>, 2016.

711